NANO LETTERS

Letter

pubs.acs.org/NanoLett

Enhanced Graphene Photodetector with Fractal Metasurface

Jieran Fang,[†,§] Di Wang,[†,§] Clayton T. DeVault,[‡,§] Ting-Fung Chung,[‡,§] Yong P. Chen,[†,‡,§] Alexandra Boltasseva,[†,§,∥] Vladimir M. Shalaev,[*,†,§] and Alexander V. Kildishev[*,†,§]

[†]School of Electrical and Computer Engineering, [‡]Department of Physics and Astronomy, and [§]Birck Nanotechnology Center and Purdue Quantum Center, Purdue University, West Lafayette, Indiana 47907, United States

[∥]DTU Fotonik, Department of Photonics Engineering, Technical University of Denmark, Lyngby, DK-2800, Denmark

Supporting Information

ABSTRACT: Graphene has been demonstrated to be a promising photodetection material because of its ultrabroadband optical absorption, compatibility with CMOS technology, and dynamic tunability in optical and electrical properties. However, being a single atomic layer thick, graphene has intrinsically small optical absorption, which hinders its incorporation with modern photodetecting systems. In this work, we propose a gold snowflake-like fractal metasurface design to realize broadband and polarization-insensitive plasmonic enhancement in graphene photodetector. We experimentally obtain an enhanced photovoltage from the fractal metasurface that is an order of magnitude greater than that generated at a plain gold−graphene edge and such an enhancement in the photovoltage sustains over the entire visible spectrum. We also observed a relatively constant photoresponse with respect to polarization angles of incident light, as a result of the combination of two orthogonally oriented concentric hexagonal fractal geometries in one metasurface.

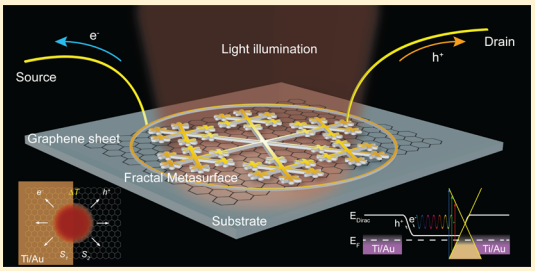

KEYWORDS: *Photodetector, graphene, fractal metasurface, plasmonics*

Graphene has been demonstrated as an appealing material for photodetection due to its unique properties such as wide optical absorption spectrum, wavelength independent absorption, high room-temperature electron and hole mobilities, mechanical flexibility, and dynamic tunability in optical and electrical properties.[1−9] So far there are primarily five known physical mechanisms that enable photodetection in graphene: the photovoltaic effect,[10−12] the photothermoelectric effect,[13−16] the bolometric effect,[17] the photogating effect,[18−20] and the surface plasmon-assisted mechanism.[21,22] Among these, the photovoltaic (PV) effect makes use of the built-in electric field that is induced by the differently doped regions in graphene to separate the optically excited electron hole pairs in graphene and give rise to photovoltage, whereas the photothermoelectric (PTE) effect is associated with the photovoltage produced by the optically generated hot electrons in regions with different thermoelectric powers (Seebeck coefficients) in graphene: $V_{PTE} = (S_1 - S_2)\Delta T$, where S_1 and S_2 are the Seebeck coefficients of two regions in graphene with different doping levels, and ΔT is the electron temperature difference across the two regions. Both effects are thought to contribute in photovoltage generation in metal−graphene−metal photodetectors (MGM-PDs),[23] and make MGM-PDs the prioritized candidates for ultrafast graphene photodetector, owing to the high carrier transport velocity[12,24] and extremely short carrier heating and cooling times[25−27] in graphene. Moreover, MGM-PDs are ideal for applications where zero power consumption and zero dark current are desired, because source drain bias and gate voltage, although useful for dynamically tuning the photogain, are not necessary for such detectors to be operative. Despite all the advantages of MGM-PDs (broadband operation, uniform sensitivity against wavelength, fast response speed, zero power consumption), the responsivity (sensitivity) in MGM-PDs is notoriously low because graphene, which absorbs merely 2.3% of incident light,[1] is used as the photoabsorption material. On the other hand, plasmon oscillations have been known and widely utilized to enhance optical absorption and generate hot electrons in various optical systems. Unsurprisingly, efforts have also been made to enhance the responsivity in MGM-PDs using plasmonic nanostructures. However, the previously proposed plasmonic enhancement methods are mostly narrowband and polarization dependent.[28−31] Optical waveguides have also been demonstrated to enhance the optical absorption by almost 100% in graphene photodetectors,[10,27] but this method requires coupling light into waveguides that could result in a bulky experimental setup. Indeed, although narrowband and polarization sensitive enhanced photodetectors are desirable in spectrally resolved and polarization specific photodetection scenarios, there is definitely a strong need for broadband and polarization insensitive enhanced photodetectors. In this work, we propose a gold fractal metasurface design that has a relatively flat optical absorption in the visible part of the spectrum to realize broadband and polarization insensitive plasmonic-enhanced graphene photodetector.

Received: August 1, 2016
Revised: December 13, 2016
Published: December 14, 2016

DOI: 10.1021/acs.nanolett.6b03202
Nano Lett. 2017, 17, 57−62

We begin by introducing a new fractal metasurface design. The metasurface is realized through a fractal tree to mimic the snowflake geometry. As demonstrated in previous works, the fractal metasurface has been shown to exhibit broadband absorption and multiple resonances with increased levels,[32−34] where the practical examples include plasmonic elements[33] that follow the Cayley tree topology[35] or the nanostructured aluminum electrodes[34] following the classical space-filling curves of Hilbert and Peano.[36,37] Here we choose the six-point asterisk shape as our seed geometry (the first-level fractal, Figure 1a). Construction of the branching is generated by

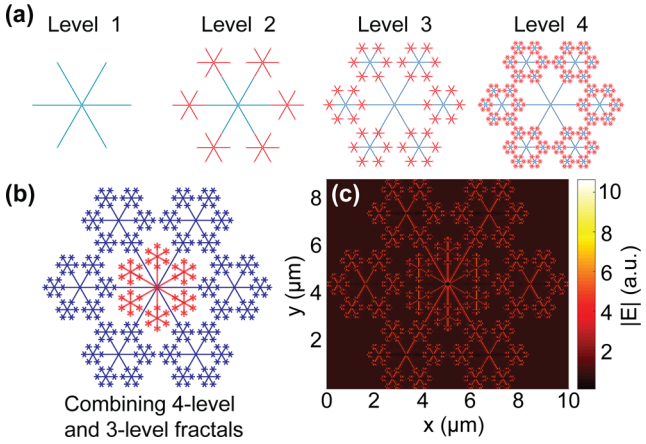

Figure 1. (a) Construction of the fractal design with "snowflake" geometry from level 1 to level 4. (b) Total structure comprising of a four-level (blue part) and a three-level (red part) fractals utilized in the study. (c) FDTD simulated in-plane electric field (of the incident electromagnetic wave) distribution just underneath the gold fractal metasurface on a glass substrate under the excitation wavelength of 530 nm. The electric field is linearly polarized along *y*-direction.

recursive iterations that is different from the classical approaches to *n*-flake generation.[35] In our case, upon each iteration six new branches are only spread from each new root point. The angle between each branch is kept at 60°. The branch width and thickness are set to be 40 nm for all levels of iterations, while branch lengths at each level are decreased by the scaling ratio of one-third as the level increases with a total level of 4, denoted by the red color in Figure 1a. For the sake of fabrication and measurement conveniences, we designed the fractal metasurface with a diameter of ∼10 μm to cover the whole area of illumination by the laser spot in our system. Nonetheless, due to the simple and inward scalability of fractal metasurfaces, it is convenient to design metasurfaces that are fitted for other spot sizes and for enhancement at other desired wavelength ranges, while keeping the overall coverage area of the metasurface unchanged with increasing fractal levels. In order to increase the density of the branches within the illumination spot and to compensate for the intrinsic polarization anisotropy, we add another three-level fractal structure concentrically with a 30° mismatch to the four-level fractal structure, denoted in red color in Figure 1b. All the arm lengths for the whole fractal metasurface are listed in Table 1.

Next, we investigate the optical characteristics of such gold fractal metasurface numerically through the finite-difference time-domain (FDTD) method.[38] We employ a dispersive model for gold, which is defined as the sum of a Drude term and two critical point terms and is implemented through a generalized dispersion material model.[39] The parameters of the

Table 1. Arm Lengths for the Whole Fractal Metasurface

level number, *N*	1	2	3	4
4-level fractal arm lengths (μm, blue segments in Figure 1b)	3.47	1.15	0.38	0.13
3-level fractal arm lengths (μm, red segments in Figure 1b)	1.39	0.46	0.15	NA

model are adopted from an online database.[40] (See Supporting Information for details.) We show one full-wave simulated in-plane electric field distribution just underneath the gold fractal metasurface when it is illuminated at the wavelength of 530 nm (Figure. 1c). The high intensity regions (hot spots) are tightly localized around the branches and edges of the fractal structures.

To further validate the performance of our metasurface, we performed near-field scanning optical microscopy (NSOM, MultiView 2000, Nanonics Imaging Ltd.) to elucidate the near-field characteristics of the plasmonic fractal. For near-field measurements, we fabricated gold fractal patterns of exactly the same dimensions on top of a bare glass substrate; this was necessary due to the strong absorption that would have otherwise occurred using a silicon substrate. The metasurface sample is illuminated from the far-field using a weakly focused 532 nm diode laser incident on the bottom of the metasurface, that is, the glass substrate side. The near-field signal is obtained by scanning a metal-coated (chromium and gold) tapered fiber with a 50 nm aperture above the surface of the sample. The scan is performed at a fixed distance of ∼100 nm in order to mitigate damage to the tip and/or sample and to eliminate topographic artifacts in the signal.[41] Figure 2a shows the

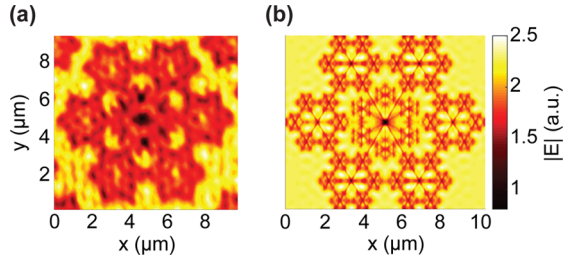

Figure 2. (a) Experimental near-field extinction map of the fractal metasurface, obtained using near-field scanning optical microscopy (NSOM). The measurement is done in collection mode at a wavelength of 532 nm. (b) The simulated electric field distribution at the wavelength of 532 nm. A floating window average is applied to mimic the 50 nm diameter aperture that is used in the NSOM experiment in (a).

experimental near-field extinction map of the metasurface. To compare with experiments, we simulated, using an FDTD method, the electromagnetic fields in a plane 100 nm above the plasmonic metasurface assuming a 532 nm plane wave incident from the substrate side and applied a moving average weighted with a 50 nm disk to account for the convolution of the tip.[42] Our results are well matched with experiment as illustrated in Figure 2b and indicate strong plasmonic extinction near the branches and edges of the fractal structure.

When visible light is incident upon the fractal metasurface, it excites plasmon oscillation in the gold fractal structure, which in turn confines and enhances the electric field of the incident electromagnetic wave within nanometers of the structure, contributing to an extensive electron−hole pair generation and elevating the electron temperature through electron−electron

DOI: 10.1021/acs.nanolett.6b03202
Nano Lett. 2017, 17, 57−62

interactions in graphene.[43] The generated carriers are then spatially separated/driven via the aforementioned built-in electric field (PV) and thermoelectric power differential (PTE) at gold−graphene interface, giving rise to a detectable photovoltage. Additionally, due to a combination of two orthogonally oriented concentric hexagonal fractal geometries in an integrated metasurface design (see Figure 1b, red and blue structures), the enhancement in photovoltage detection is independent of the polarization angle of the incident electromagnetic wave, providing yet another feature unprecedented by the previously reported plasmonic enhanced MGM-PDs.

In our experiment, we integrated the fractal metasurface with the drain contact of the graphene field effect transistor (FET) device, so that the metasurface is at the same electrical potential as the bulk drain contact to facilitate the electron (hole) collection and also the theoretical analysis. The device fabrication starts with the transfer of a monolayer graphene sheet[44] grown by chemical vapor deposition (CVD) onto a highly p-doped silicon substrate (0.001−0.005 Ω-cm) with a 300 nm thick dry thermal dioxide on top. The fractal metasurface with gold rod for electrical connection with the drain contact and a ring encircling the fractal metasurface to maximize electron (hole) harvesting at the source contact were defined by electron beam lithography (EBL), Ti (3 nm)/Au (40 nm) metallization and liftoff. The large sheet of graphene was then etched into smaller rectangles using photolithography and O_2 plasma etch. The bulk source and drain contact pads (3 nm Ti, 80 nm Au) were fabricated to directly cover the gold rods and partially the graphene sheet. Finally wire bonding the fabricated chip to printed circuit board was performed for electrical measurements.

The photovoltage response of our device was measured by the setup illustrated in Figure 3a. A continuous wave laser (Ar−Kr) chopped at 1.1 kHz by an optical chopper was coupled to a 10× microscope and was then focused on the photodetector with a spot diameter of ∼7 μm. The generated photovoltage was then measured via the source−drain contacts by a lock-in amplifier synchronized with the optical chopper. We first investigated the enhancement in photovoltage generation from the ring encircling the fractal metasurface. To do this, on sample 1 we fabricated a tip-and-ring structure without fractal metasurface and placed it in parallel with the structure with fractal metasurface (see Figure 3b). By measuring the photovoltage generated on the tip ("spot B" in Figure 3b) and on the plain gold-graphene edge ("spot C" in Figure 3b), we observed an average of ∼5 times photovoltage enhancement on the tip. We then measured the photovoltage generated when the laser spot was incident upon the fractal metasurface ("spot A" in Figure 3b), denoted as $V_{fractal}$, and when the laser spot was incident upon the plain gold−graphene edge ("spot C" in Figure 3b), denoted as V_{edge}, and defined $V_{fractal}/V_{edge}$ as the enhancement factor of photovoltage generated on fractal metasurface to plain edge. The study of fractal metasurface photovoltage generation was carried out at six experimentally available wavelengths, 476, 488, 514, 530, 568, and 647 nm, to investigate the broadband enhancement effect in the visible spectrum. In this work, all measurements were done with zero gate voltage ($V_G = 0$) and source−drain bias ($V_{SD} = 0$), unless otherwise indicated. As an illustration, we show the photovoltage generated as a function of incident power at the wavelength of 568 nm in Figure 3c,d (the measurements at other wavelengths are provided in the Supporting Information),

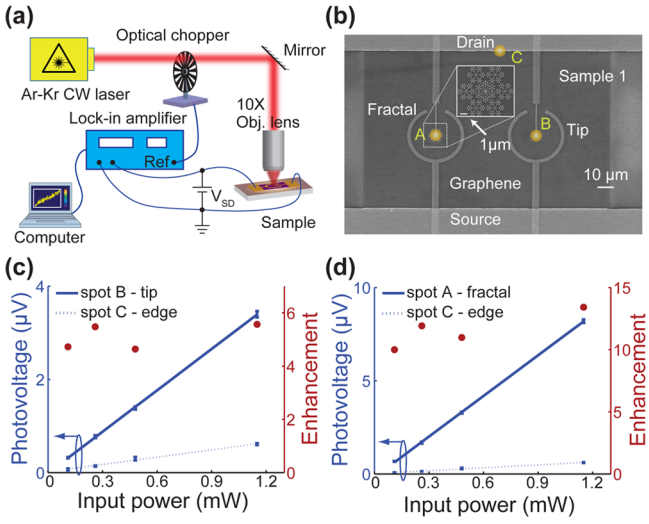

Figure 3. (a) Experimental setup for photovoltage measurement; (b) scanning electron micrograph (SEM) of sample 1 the graphene photodetector with the fractal metasurface and tip-and-ring structure (the white scale bar is 10 μm); inset image shows the zoomed-in view of gold fractal metasurface (the white scale bar is 1 μm). (c) Blue lines with error bars: measured photovoltage when laser is incident on tip without fractal metasurface (spot B in (b), solid line) and on plain edge (spot C in (b), dotted line) as a function of incident power, the error bars are experimentally measured data points and blue lines are linear fits to the experimental data. Red circles: enhancement factors from tip to edge at individual tested incident powers. (d) Similar to (c), the measured photovoltage generated on fractal metasurface (spot A in (b), solid blue line) and on plain metal/graphene edge (spot C in (b), dashed blue line) as a function of incident power and enhancement factors (red dots, right vertical axis) at each tested power. The measurements in (c,d) were carried out at the wavelength of 568 nm.

from which a linear relationship between the two can be seen, indicating that we were operating the device before absorption saturation.[29]

To show the broadband nature of the photovoltage enhancement, we plot the enhancement factors $V_{fractal}/V_{edge}$ at the six tested wavelengths in Figure 4a. The error bars come from the fact that the enhancement factors vary with varying incident optical powers. As is evident in Figure 4a, enhancement factors ranging from 10 to 16 are achieved at the tested visible-spectrum wavelengths. We notice that although the simulated optical absorption of the fractal metasurface is rather flat in the investigated spectral range (shown by the cyan solid line in Figure 4a), the enhancement factors in photovoltage generation exhibit slight wavelength dependence and the enhancement factors increase with increasing wavelength. We believe that the reason for such behavior is two-fold. On one hand, it is caused by the greater photovoltage generated on the plain gold−graphene edge at shorter wavelengths due to stronger heating of gold pad, accounted for by the PTE effect in photovoltage generation. On the fractal metasurface, the entire metasurface area contributes to generating photovoltage ($V_{fractal}$), independent of incident light wavelength. On the plain gold−graphene edge (V_{edge}), however, larger/smaller area extending into the gold pad within the laser spot contributes to generating photovoltage at respectively shorter/longer wavelengths.[23,26] As a result, the enhancement factors decrease at shorter wavelengths simply because the area of graphene that contributes to V_{edge} increases compared to that at longer

DOI: 10.1021/acs.nanolett.6b03202
Nano Lett. 2017, 17, 57−62

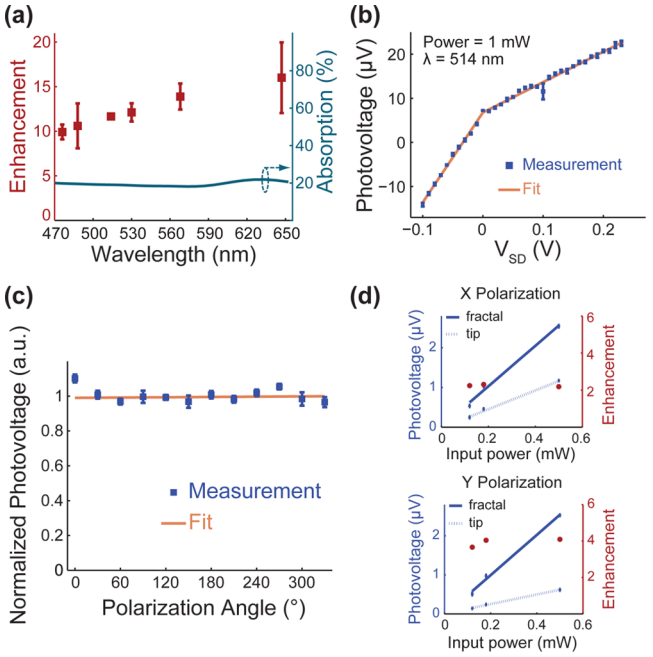

Figure 4. (a) Red markers with error bars: measured enhancement of photovoltage generation ($V_{fractal}/V_{edge}$, spot A to spot C in Figure 3b) over a wavelength range from 476 to 647 nm. Cyan curve: the simulated absorption spectrum of the fractal metasurface. (b) Measured photovoltage as a function of source drain bias V_{SD}. Measurement was done at the wavelength of 514 nm with an input power of 1 mW. Blue markers are measured data points and orange curve is linear fit to the data points. (c) Normalized photovoltage as a function of incident light polarization angles. Blue markers are measured data points and orange curve is linear fit to the data points. (d) Blue lines: measured photovoltage generated on fractal metasurface (spot A in Figure 3b, solid lines) and on tip (spot B in Figure 3b, dashed lines) with *x*-polarized light (upper panel) and *y*-polarized light (lower panel). See Figure 1c for *x*- and *y*-directions.

wavelength, while it remains identical across the entire tested wavelength range for $V_{fractal}$. On the other hand, the Ti doping and intrinsic p-doping in bulk graphene induces p−p junction at the metal/graphene interface, where PV and PTE effects counteract with each other.[13,15] The competition between the two effects could also be a reason for the increasing trend of enhancement factors with wavelength.

It is also known that the source−drain bias in graphene photodetectors can alter the band bending across the graphene FET device, making it a handy mechanism to tune the photovoltage responsivity. We show in Figure 4b that the amplitude of the photovoltage increases monotonically with increasing source−drain bias and the photovoltage can be tuned up to 24 μV, three times of that at zero bias. We did not observe reduced responsivity up to V_{SD} = 0.25 V, indicating that the breakdown field of the graphene channel, which is the limit of the bias that can be applied to the device, has not been reached. In Figure 4c, we show that the photoresponse is insensitive to the polarization angle of incident light, as is expected from the aforementioned hexagonally symmetric geometry of the fractal metasurface design. The two panels in Figure 4d indicate that the fractal metasurface provides more polarization robustness over the tip-and-ring structure which exhibits 50% drop in responsivity when light is polarized in the *y*-direction. We simulated the absorption spectrum of the metasurface under 0° (E-field along *x*-axis in Figure 1c) and 90° (E-field along *y*-axis in Figure 1c) polarizations and observe only negligible difference between the two (see Supporting Information). The experimental and simulation results demonstrate the robustness of the photovoltage enhancement by the proposed fractal metasurface with respect to polarization of incident light.

In order to compensate for the partial enhancement due to the reduced source-drain distance for spot A in sample 1, we fabricated sample 2 where we placed a fractal metasurface encircled by a 30 μm ring in parallel with a plain source−drain structure with 30 μm separation on the same graphene sheet and studied the enhancement of photovoltage between the two structures. Similar to sample 1, in sample 2 we study the ratio of photovoltage generated when laser is incident on fractal metasurface (spot A in Figure 5a) to that generated when

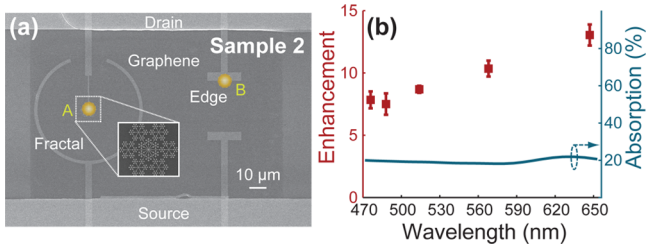

Figure 5. (a) Scanning electron micrograph (SEM) of the graphene photodetector sample 2 with the fractal metasurface (the white scale bar is 10 μm) encircled by 30 μm ring and source-drain contacts separated by 30 μm; inset image shows the zoomed-in view of gold fractal metasurface. Similar to sample 1, the ratio of the photovoltage generated on spot A to that generated on spot B is defined as the enhancement factor. (b) Similar to Figure 4a, the measured enhancement of photovoltage generation (red markers with error bars, left vertical axis) from 476 to 647 nm and the simulated absorption spectrum of the fractal metasurface (cyan curve, right vertical axis) on sample 2.

laser is incident on one of the 30 μm separated source drain contacts (spot B in Figure 5a), where the maximum photovoltage happens in pristine MGM-PDs.[45,46] In Figure 5b, we plot the enhancement factors at five tested wavelengths for sample 2. It can be seen that although the enhancement factors are reduced compared to those of sample 1, they are still close to 10 and can be as large as 13 at longer wavelengths.

In conclusion, by reforming the source and drain contacts into a fractal metasurface and a ring encircling it, we demonstrated a broadband graphene photodetector exhibiting enhancement factors of 8−13 over the visible spectrum. The application of the fractal metasurface is not bound to graphene photodetectors but can also be integrated with PV/PTE photodetectors made of other photodetection materials.[47−50] The great flexibility of our fractal metasurface design enables broadband enhancement at other portions of the electromagnetic spectrum[51] and for various spot sizes. Additionally, the photoresponse enhancement is insensitive to the incident light polarization, a quintessential feature of a practical photodetecting/photoharvesting system. These attributes, combined with dynamic tunability through source drain bias, make our fractal metasurface an advancement toward the incorporation of graphene into modern photodetecting and photoharvesting applications.

DOI: 10.1021/acs.nanolett.6b03202
Nano Lett. 2017, 17, 57−62

■ ASSOCIATED CONTENT

Supporting Information

The Supporting Information is available free of charge on the ACS Publications website at DOI: 10.1021/acs.nanolett.6b03202.

The dispersion of Au used in the numerical model, the photovoltage enhancement measurements at all tested wavelengths for samples 1 and 2, the numerical simulation of the fractal metasurface's optical response under orthogonal light polarizations, the graphene doping level analysis, and the gate voltage dependence of photovoltage generated on fractal metasurface (PDF)

■ AUTHOR INFORMATION

Corresponding Authors

*E-mail: shalaev@purdue.edu.
*E-mail: kildishev@purdue.edu.

ORCID

Jieran Fang: 0000-0002-4731-0482
Di Wang: 0000-0002-3536-7027

Author Contributions

J.F. and D.W. contributed equally to this work. The manuscript was written through contributions of all authors. All authors have given approval to the final version of the manuscript.

Funding

NSF Materials Research Science and Engineering Center (MRSEC) program (DMR 1120923), NSF Civil, Mechanical, and Manufacturing Innovation (CMMI) program (1538360) for graphene synthesis, U.S. Army Research Office Grant 63133-PH (W911NF-13-1-0226), and the Air Force Office of Scientific Research MURI Grant (FA9550-14-1-0389)

Notes

The authors declare no competing financial interest.

■ ACKNOWLEDGMENTS

The authors would like to acknowledge fruitful discussions with M. A. Alam and J. Appenzeller. D.W. would like to thank Y. Xuan for helpful instructions on fabrication of the samples by E-beam lithography.

■ REFERENCES

(1) Nair, R. R.; Grigorenko, A. N.; Blake, P.; Novoselov, K. S.; Booth, T. J.; Peres, N. M. R.; Stauber, T.; Geim, A. K. *Science* **2008**, *320* (5881), 1308.
(2) Li, Z. Q.; Henriksen, E. a.; Jiang, Z.; Hao, Z.; Martin, M. C.; Kim, P.; Stormer, H. L.; Basov, D. N. *Nat. Phys.* **2008**, *4* (7), 532−535.
(3) Emani, N. K.; Chung, T.-F.; Ni, X.; Kildishev, A. V.; Chen, Y. P.; Boltasseva, A. *Nano Lett.* **2012**, *12* (10), 5202−5206.
(4) Fang, Z.; Thongrattanasiri, S.; Schlather, A.; Liu, Z.; Ma, L.; Wang, Y.; Ajayan, P. M.; Nordlander, P.; Halas, N. J.; García de Abajo, F. J. *ACS Nano* **2013**, *7* (3), 2388−2395.
(5) Tielrooij, K. J.; Orona, L.; Ferrier, A.; Badioli, M.; Navickaite, G.; Coop, S.; Nanot, S.; Kalinic, B.; Cesca, T.; Gaudreau, L.; Ma, Q.; Centeno, A.; Pesquera, A.; Zurutuza, A.; de Riedmatten, H.; Goldner, P.; García de Abajo, F. J.; Jarillo-Herrero, P.; Koppens, F. H. L. *Nat. Phys.* **2015**, *11* (3), 281−287.
(6) Emani, N. K.; Wang, D.; Chung, T.-F.; Prokopeva, L. J.; Kildishev, A. V.; Shalaev, V. M.; Chen, Y. P.; Boltasseva, A. *Laser Photon. Rev.* **2015**, *9* (6), 650−655.
(7) Lee, G.-H.; Yu, Y.-J.; Cui, X.; Petrone, N.; Lee, C.-H.; Choi, M. S.; Lee, D.-Y.; Lee, C.; Yoo, W. J.; Watanabe, K.; Taniguchi, T.; Nuckolls, C.; Kim, P.; Hone, J. *ACS Nano* **2013**, *7* (9), 7931−7936.
(8) Lee, C.-H.; Lee, G.; van der Zande, A. M.; Chen, W.; Li, Y.; Han, M.; Cui, X.; Arefe, G.; Nuckolls, C.; Heinz, T. F.; Guo, J.; Hone, J.; Kim, P. *Nat. Nanotechnol.* **2014**, *9* (9), 676−681.
(9) Emani, N. K.; Kildishev, A. V.; Shalaev, V. M.; Boltasseva, A. *Nanophotonics* **2015**, *4* (1), 214−223.
(10) Gan, X.; Shiue, R.-J.; Gao, Y.; Meric, I.; Heinz, T. F.; Shepard, K.; Hone, J.; Assefa, S.; Englund, D. *Nat. Photonics* **2013**, *7* (11), 883−887.
(11) Mueller, T.; Xia, F.; Avouris, P. *Nat. Photonics* **2010**, *4* (5), 297−301.
(12) Xia, F.; Mueller, T.; Lin, Y.; Valdes-Garcia, A.; Avouris, P. *Nat. Nanotechnol.* **2009**, *4* (12), 839−843.
(13) Gabor, N. M.; Song, J. C. W.; Ma, Q.; Nair, N. L.; Taychatanapat, T.; Watanabe, K.; Taniguchi, T.; Levitov, L. S.; Jarillo-Herrero, P. *Science* **2011**, *334* (6056), 648−652.
(14) Lemme, M. C.; Koppens, F. H. L.; Falk, A. L.; Rudner, M. S.; Park, H.; Levitov, L. S.; Marcus, C. M. *Nano Lett.* **2011**, *11* (10), 4134−4137.
(15) Song, J. C. W.; Rudner, M. S.; Marcus, C. M.; Levitov, L. S. *Nano Lett.* **2011**, *11* (11), 4688−4692.
(16) Ghahari, F.; Xie, H. Y.; Taniguchi, T.; Watanabe, K.; Foster, M. S.; Kim, P. *Phys. Rev. Lett.* **2016**, *116* (13), 1−5.
(17) Freitag, M.; Low, T.; Xia, F. N.; Avouris, P. *Nat. Photonics* **2012**, *7* (1), 53−59.
(18) Liu, C.-H.; Chang, Y.-C.; Norris, T. B.; Zhong, Z. *Nat. Nanotechnol.* **2014**, *9* (4), 273−278.
(19) Konstantatos, G.; Badioli, M.; Gaudreau, L.; Osmond, J.; Bernechea, M.; de Arquer, F. P. G.; Gatti, F.; Koppens, F. H. L. *Nat. Nanotechnol.* **2012**, *7* (6), 363−368.
(20) Fang, Z.; Wang, Y.; Liu, Z.; Schlather, A.; Ajayan, P. M.; Koppens, F. H. L.; Nordlander, P.; Halas, N. J. *ACS Nano* **2012**, *6* (11), 10222−10228.
(21) Spirito, D.; Coquillat, D.; De Bonis, S. L.; Lombardo, A.; Bruna, M.; Ferrari, A. C.; Pellegrini, V.; Tredicucci, A.; Knap, W.; Vitiello, M. S. *Appl. Phys. Lett.* **2014**, *104* (6), 061111.
(22) Koppens, F. H. L.; Mueller, T.; Avouris, P.; Ferrari, a C.; Vitiello, M. S.; Polini, M. *Nat. Nanotechnol.* **2014**, *9* (10), 780−793.
(23) Echtermeyer, T. J.; Nene, P. S.; Trushin, M.; Gorbachev, R. V.; Eiden, A. L.; Milana, S.; Sun, Z.; Schliemann, J.; Lidorikis, E.; Novoselov, K. S.; Ferrari, A. C. *Nano Lett.* **2014**, *14* (7), 3733−3742.
(24) Brenneis, A.; Gaudreau, L.; Seifert, M.; Karl, H.; Brandt, M. S.; Huebl, H.; Garrido, J. A.; Koppens, F. H. L.; Holleitner, A. W. *Nat. Nanotechnol.* **2014**, *10* (2), 135−139.
(25) Tielrooij, K. J.; Piatkowski, L.; Massicotte, M.; Woessner, a; Ma, Q.; Lee, Y.; Myhro, K. S.; Lau, C. N.; Jarillo-Herrero, P.; van Hulst, N. F.; Koppens, F. H. L. *Nat. Nanotechnol.* **2015**, *10* (5), 437−443.
(26) Tielrooij, K. J.; Massicotte, M.; Piatkowski, L.; Woessner, a; Ma, Q.; Jarillo-Herrero, P.; van Hulst, N. F.; Koppens, F. H. L. *J. Phys.: Condens. Matter* **2015**, *27* (16), 164207.
(27) Shiue, R. J.; Gao, Y.; Wang, Y.; Peng, C.; Robertson, A. D.; Efetov, D. K.; Assefa, S.; Koppens, F. H. L.; Hone, J.; Englund, D. *Nano Lett.* **2015**, *15* (11), 7288−7293.
(28) Echtermeyer, T. J.; Britnell, L.; Jasnos, P. K.; Lombardo, A.; Gorbachev, R. V.; Grigorenko, A. N.; Geim, A. K.; Ferrari, A. C.; Novoselov, K. S. *Nat. Commun.* **2011**, *2*, 458.
(29) Yao, Y.; Shankar, R.; Rauter, P.; Song, Y.; Kong, J.; Loncar, M.; Capasso, F. *Nano Lett.* **2014**, *14* (7), 3749−3754.
(30) Liu, Y.; Cheng, R.; Liao, L.; Zhou, H.; Bai, J.; Liu, G.; Liu, L.; Huang, Y.; Duan, X. *Nat. Commun.* **2011**, *2*, 579.
(31) Freitag, M.; Low, T.; Zhu, W.; Yan, H.; Xia, F.; Avouris, P. *Nat. Commun.* **2013**, *4*, 1951.
(32) Shalaev, V. M. *Nonlinear optics of random media: fractal composites and metal-dielectric films*; Springer Science & Business Media: New York, 1999; Vol. *158*.
(33) Gottheim, S.; Zhang, H.; Govorov, A. O.; Halas, N. J. *ACS Nano* **2015**, *9* (3), 3284−3292.
(34) Afshinmanesh, F.; Curto, A. G.; Milaninia, K. M.; van Hulst, N. F.; Brongersma, M. L. *Nano Lett.* **2014**, *14* (9), 5068−5074.
(35) Lin, Y.; Zhang, Z. *J. Chem. Phys.* **2013**, *138* (9), 094905.

DOI: 10.1021/acs.nanolett.6b03202
Nano Lett. 2017, 17, 57−62

(36) Bader, M. *Space-filling curves: an introduction with applications in scientific computing*; Springer Science & Business Media: New York, 2012; Vol. *9*.
(37) Sagan, H. *Space-filling curves*; Springer Science & Business Media: New York, 2012.
(38) Taflove, A.; Hagness, S. *Computational Electrodynamics: The Finite-Difference Time-Domain Method*; Artech House: Norwood, MA, 2005.
(39) Prokopeva, L. J.; Borneman, J. D.; Kildishev, A. V. *IEEE Trans. Magn.* **2011**, *47*, 1150−1153.
(40) Ni, X.; Liu, Z.; Kildishev, A. V. *PhotonicsDB: Optical Constants* **2008**, DOI: 10.4231/D3FT8DJ4J.
(41) Hecht, B.; Bielefeldt, H.; Inouye, Y.; Pohl, D. W.; Novotny, L. *J. Appl. Phys.* **1997**, *81* (6), 2492−2498.
(42) Bakker, R.; Boltasseva, A.; Liu, Z.; Pedersen, R. H.; Gresillon, S.; Kildishev, A. V.; Drachev, V. P.; Shalaev, V. M. *Opt. Express* **2007**, *15* (21), 13682−13688.
(43) Graham, M. W.; Shi, S.-F.; Ralph, D. C.; Park, J.; McEuen, P. L. *Nat. Phys.* **2012**, *9* (2), 103−108.
(44) Chung, T.; Shen, T.; Cao, H. *Int. J. Mod. Phys. B* **2013**, *27* (10), 1341002.
(45) Mueller, T.; Xia, F.; Freitag, M.; Tsang, J.; Avouris, P. *Phys. Rev. B: Condens. Matter Mater. Phys.* **2009**, *79* (24), 245430.
(46) Lee, E. J. H.; Balasubramanian, K.; Weitz, R. T.; Burghard, M.; Kern, K. *Nat. Nanotechnol.* **2008**, *3* (8), 486−490.
(47) Massicotte, M.; Schmidt, P.; Vialla, F.; Schädler, K. G.; Reserbat-Plantey, A.; Watanabe, K.; Taniguchi, T.; Tielrooij, K. J.; Koppens, F. H. L. *Nat. Nanotechnol.* **2015**, *11*, 42−46.
(48) Lei, S.; Wen, F.; Ge, L.; Najmaei, S.; George, A.; Gong, Y.; Gao, W.; Jin, Z.; Li, B.; Lou, J.; Kono, J.; Vajtai, R.; Ajayan, P.; Halas, N. J. *Nano Lett.* **2015**, *15* (5), 3048−3055.
(49) Wang, W.; Klots, A.; Prasai, D.; Yang, Y.; Bolotin, K. I.; Valentine, J. *Nano Lett.* **2015**, *15* (11), 7440−7444.
(50) Buscema, M.; Groenendijk, D. J.; Blanter, S. I.; Steele, G. A.; van der Zant, H. S. J.; Castellanos-Gomez, A. *Nano Lett.* **2014**, *14* (6), 3347−3352.
(51) Knight, M. W.; Sobhani, H.; Nordlander, P.; Halas, N. J. *Science* **2011**, *332* (6030), 702−704.

DOI: 10.1021/acs.nanolett.6b03202
Nano Lett. 2017, 17, 57−62